



## The influence of doping on flash sintering conditions in $\text{SrTi}_{1-x}\text{Fe}_x\text{O}_{3-\delta}$

Neta Shomrat<sup>a</sup>, Sioma Baltianski<sup>b</sup>, Elad Dor<sup>b</sup>, Yoed Tsur<sup>a,b,\*</sup>

<sup>a</sup> The Nancy & Stephen Grand Technion Energy Program (GTEP), Technion- Israel Institute of Technology, Haifa 3200003, Israel

<sup>b</sup> Chemical Engineering Department, Technion- Israel Institute of Technology, Haifa 3200003, Israel



### ARTICLE INFO

#### Article history:

Received 3 May 2016

Received in revised form 21 July 2016

Accepted 28 July 2016

Available online 13 August 2016

#### Keywords:

Flash-sintering  
Heat balance equation  
Strontium titanate  
Green body resistance  
Onset temperature

### ABSTRACT

Joule heating in flash sintering depends on the sample resistance, which is linked to the charged defects concentration. To study the contribution of defects on the flash sintering mechanism, this link should be untied. In  $\text{SrTi}_{1-x}\text{Fe}_x\text{O}_{3-\delta}$  (STFO) system, point defect concentration can be pinned while the resistance is influenced by the oxygen partial pressure ( $p_{\text{O}_2}$ ).  $\text{SrTi}_{0.97}\text{Fe}_{0.03}\text{O}_{2.985}$  onset temperature at different  $p_{\text{O}_2}$  was examined at constant oxygen vacancy concentration. The furnace onset temperature decreases with increasing  $p_{\text{O}_2}$ . The onset temperature of five STFO samples was predicted based on resistance-temperature dependency of the porous green ceramics in a dynamic heat balance simulation. High compatibility of model and experimental results showed reduction of onset temperature with increasing doping. Ex-situ impedance measurements of green samples reveal an overlapping Nyquist plots close to the sample onset temperature. This indicates that the onset is determined by the green body resistance regardless how it has been achieved.

© 2016 Elsevier Ltd. All rights reserved.

## 1. Introduction

The innovative flash sintering process raised a great interest in the past few years due to its applicability in various engineering fields and the interesting scientific questions it evokes. Unlike unconventional sintering processes such as hot press, microwave sintering and spark plasma sintering, flash sintering reduces the process duration to seconds and allows sintering at much lower temperatures. The fact that it is such a time and energy beneficial procedure makes it cost effective and highly applicable in all ceramic production industries, such as solid oxide fuel cells, battery electrodes, membranes, capacitors etc. Additionally, since it is a rapid technique at relatively low temperatures it is also the solution for sintering materials with highly volatile components that are hard to densify [1]. This process has a number of controllable parameters: the applied voltage and its type (AC/DC) [2,3]; the maximal power compliance and the “switching” conditions; the furnace temperature; and the green body properties. The initial powder is characterized by its own transport and physical properties namely, electrical conductivity, thermal conductivity and thermal expansion. It was shown that by determine different parameters of the

system, one can control the obtained ceramic grain size [4] and final density [5].

The process can be subdivided into three distinguishable stages under applied electric field [6]. In the first stage (incubation), a constant voltage is applied on the sample electrodes, a rapid increase of the current is observed due to a sharp resistivity fall, accompanied with an increase of the sample temperature. The second stage is a transient stage at which the current reaches the instrument compliance value and the power source must be switched from voltage-control to current-control, to decelerate the electrical runaway. A typical power density peak is indicative at this stage, followed by an abrupt shrinkage. The third stage is still under current-control, but can be defined as a steady-state regime with a constant power density and only moderate shrinkage.

The onset conditions are defined as the furnace temperature and applied field above which the flash sintering process occurs. The onset conditions are therefore a threshold required for the flash occurrence. These onset conditions vary between different materials; the ability to predict them could not only be handful when working with new materials, but also may shed light on the mechanisms that govern the process.

The nature of unusual flash sintering behavior is evoking scientific questions and various advanced researches regarding its mechanism. The prominent phenomenon was initially explained by Raj [7] claiming the rise in sample temperature during incubation is a result of the Joule heating produced from a sharp increase in the conductivity. Raj model [6] of Joule heating and black body

\* Corresponding author at: Chemical Engineering Department, Technion- Israel Institute of Technology, Haifa 3200003, Israel.

E-mail addresses: [snet@tx.technion.ac.il](mailto:snet@tx.technion.ac.il) (N. Shomrat), [\(Y. Tsur\)](mailto:tsur@technion.ac.il).

radiation, took into account the energy losses by radiation (assuming that convection and conduction contributions can be neglected) to predict the sample temperature as a function of the power density at steady state. The conclusion was that even in case where the sample temperature at the power spike (stage II) reaches temperatures close to conventional sintering conditions, it lasts only a few seconds. This “flash” is not sufficient to sinter the entire bulk sample. It was concluded that Joule heating alone could not explain the process of flash sintering. The mechanism of flash sintering should provide an explanation regarding the non-linear electrical conductivity and rapid mass transport kinetics.

Several models [8–15], based on energy conservation, described the process properties and contributed to our current understanding of the mechanism. Todd et al., [14] showed that the electrical and thermal properties of 3YSZ flash conditions can be predicted by the resistivity-temperature relationship of the green body sample with no adjustable parameters. The flash occurrence is primarily caused by runaway Joule heating. Two models which simulate the thermal runaway supported this result: a static one with uniform temperature (SU) and a dynamic one with non-uniform temperature (DNU). Comparing the two models with experimental results on 3YSZ showed that both models are highly compatible with experimental results at different setups. Moreover, their DNU model predicted successfully the current behavior and duration of the incubation stage. The DNU model also provides evidence for inhomogeneity in the sample temperature during the abrupt heating rates and even during the constant current stage. Grasso et al., [10] presented the temperature distribution inside the sample under flash, using simulation based on finite element method. They showed that under a constant electric field, local sample overheating is observed that reaches equilibrium rapidly. In their simulation, the core of the sample reaches high temperatures, while the edges are approximately at 500 °C colder. This result raises important questions regarding the homogeneity of the obtained dense sample and its thermal stresses.

Dong et al. [9] model also agrees with the above conclusion in which Joule heating is the cause for the thermal runaway and consequently drives the process by creating a positive feedback under voltage control. In their time-dependent model [15] they predicted the furnace onset temperature by solving the heat transfer equation while separating two distinguishable regimes. A ‘radiation heating control’ at which Joule heating is insignificant and a ‘Joule heating control’ regime where a thermal runaway occurs. They have defined a switchover condition—where Joule heating rate equals the radiation rate. Both the heat transfer model and the switchover condition predicated the onset temperature accurately. Zhang et al. [15] have been able to predict the onset temperature of ZnO, both single crystal and powder, while including in their model the heat dissipation from conduction and convection in addition to radiation. Interestingly enough, they showed that bismuth doping has increased the onset temperature. A dynamic model based on bifurcation criterion successfully predicted the onset temperature [11].

While Joule heating has been proven to have the major contribution to flash sintering initiation, lattice defects and their transport properties are also influenced by the applied field and play an important role in the process initiation and in the densification. Long and short range interactions between lattice defects, such as Frenkel defect nucleation [4,6], Ruddlesden-Popper phases [5] and segregation of vacancies [16], invoked as possible contributions to flash sintering.

Charged defects do affect the flash process; their effect could be a result of two avenues, electrical and thermal. Electrical: charged defects nature and concentration affect the sample resistance, which is linked to Joule heating. Thermal: transport properties, which are usually linked to temperature through Arrhenius behavior, enhance microstructure evolution and accelerate sintering [17].

The question is whether these two contributions of defects can be analyzed separately?

$\text{SrTi}_{1-x}\text{Fe}_x\text{O}_{3-\delta}$  (STFO) is a model mixed ionic electronic conductor (MIEC) [18,19] with a simple cubic structure. Its defects model and expansion behavior are widely investigated [20,21]. Moreover it was successfully flash sintered before at different conditions [22]. In Iron doped  $\text{SrTiO}_3$ , the compensation for substituting titanium with iron can be either electronic (by holes) or ionic (by oxygen vacancies). The concept of doping factor can be used to determine the partition of these modes of compensation [23,24]. The doping factor,  $f$ , is defined as the ratio between the quasi-free electron concentration at a reference state,  $n_0$ , and a new concentration,  $n$ , after introducing a dopant to the system. All the parameters of the intrinsic material in the reference state (subscript 0), such as native defect concentration, as well as the conditions of temperature and oxygen partial pressure should be well defined:

$$n = fn_0 \quad 0 < f < 1 \text{ in case of acceptor dopant.} \quad (1)$$

In the reference state, the main native point defects are anion vacancies  $V_O^{''}$ , cation vacancies  $V_{\text{Sr}}^{''}$  and  $V_{\text{Ti}}^{'''}$ , electrons and holes. The neutrality equation is:

$$n_0 + 6V_i = p_0 + 2[V_O^{''}]_0 \quad (2)$$

where  $p_0$  is the electron holes concentration at the reference state,  $V_i$  represents the concentration of both cation vacancies in the reference, stoichiometric, state. After doping with acceptors, the new neutrality equation, written in terms of doping factor, indicates that when the doping is increased the concentration of oxygen vacancies is increased by a factor off<sup>-2</sup> ( $f < 1$ ).

$$[Fe_{\text{Ti}}'] + fn_0 + 6V_i = f^{-1}p_0 + 2f^{-2}[V_O^{''}]_0 \quad (3)$$

Therefore, by increasing iron doping, the oxygen vacancy concentration increases at a higher rate than the hole concentration and is eventually pinned by the dopant concentration. The influence of oxygen vacancies on the initial step of sintering was widely reported, e.g. for YSZ [25] and doped  $\text{BaTiO}_3$  [17]. It was shown that enhancing their concentration lowers the temperature of the early-stage sintering.

This work contains two parts. First we simulate the dynamic energy balance during the incubation stage and at the steady state stage. This energy balance allows us to predict the required furnace onset temperature ( $T_\infty$ ) as well as the sample average temperature ( $T_s$ ) at any time, notably at the power spike. The novelty in this part is the ability and demonstration to simulate the process using properties that were measured experimentally on the same flash sintering system, assembled in a dilatometer<sup>1</sup>. Accordingly, the simulation is performed specifically for the dilatometer configuration. Pre-fitting Arrhenius equation to measured resistance data, provides the activation energy and the pre-exponential factor of Arrhenius equation which are rarely reported for green body samples and enhance the model accuracy. In addition, the convection and conduction heat transport compatible to our system are taken into consideration. We examined the onset temperature of five different doped samples of  $\text{SrTi}_{1-x}\text{Fe}_x\text{O}_{3-\delta}$  ( $x = 0, 0.1, 0.5, 1$  and  $3\%$ ) (STFO). The model results were compared to the measured onset temperatures of the STFO samples, showing that the furnace onset temperature is decreased with increasing iron content and can be predicted solely from solving the heat balance equation.

Second, to evaluate the direct contribution of oxygen vacancies on the onset temperature (apart from its influence on the resistance), the onset temperature of  $\text{SrTi}_{0.97}\text{Fe}_{0.03}\text{O}_{2.985}$  was examined at different  $p\text{O}_2$ . In highly doped samples, such as  $\text{SrTi}_{0.97}\text{Fe}_{0.03}\text{O}_{2.985}$ , the concentration of oxygen vacancies remain almost unchanged over a wide range of  $p\text{O}_2$  and temperatures, while the resistance varies [20]. This allows us to examine the

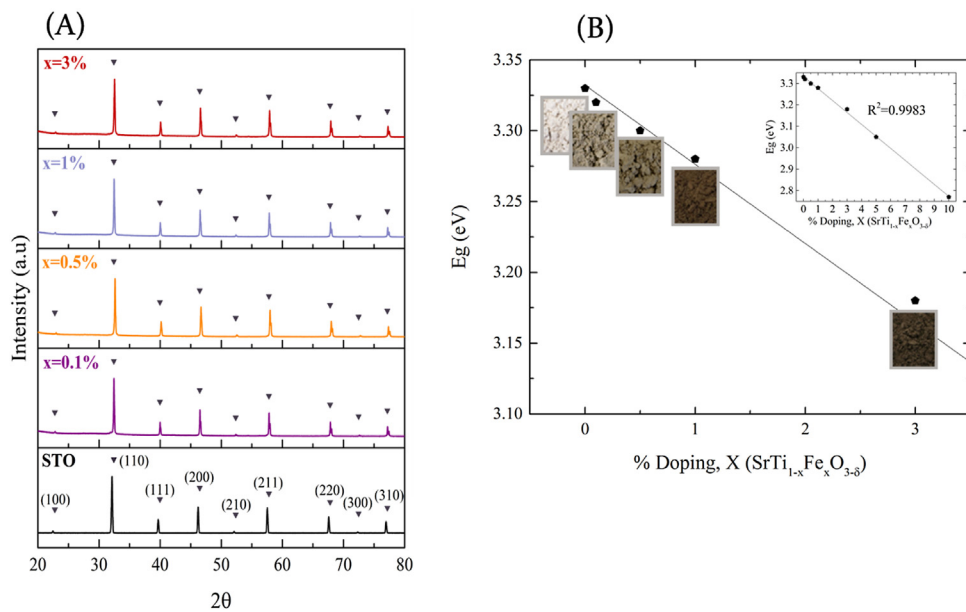


**Fig. 1.** (A) XRD pattern of STFO powders prepared by solid-state reaction. The pattern is compared to cubic SrTiO<sub>3</sub>. All peaks at all STFO powders correspond to cubic STO with no detected impurities. (B) Optical band gap, E<sub>g</sub>, of STFO powders. Higher iron concentration STFO are shown in the inset to highlight that the linear trend is kept toward highly doped samples. The images of the STFO powders indicated the presence of iron, which expressed in a darker powder as iron content is increased. The dependence follows a linear trend line that confirm the nominal composition. HR-SEM images did not reveal any change in the grain size or shape with increasing iron content up to 3%.

effect of Joule heating on the onset temperature when the sample resistance changes but the oxygen vacancy concentration does not.

## 2. Materials and methods

### 2.1. Materials

A series of SrTi<sub>1-x</sub>Fe<sub>x</sub>O<sub>3-δ</sub> powders ( $x = 0, 0.1\%, 0.5\%, 1\%, 3\%, 5\%$ ) were prepared by conventional solid state reaction. Corresponding molar ratios of SrCO<sub>3</sub> (99.995%, Sigma Aldrich, USA), TiO<sub>2</sub> (99.99%, Sigma Aldrich, Japan) and Fe<sub>2</sub>O<sub>3</sub> (>99.995%, Sigma Aldrich, UK) were ball-milled in the DDW for 24 h at 300 rpm. The suspensions were dried in a vacuum furnace, followed by hand milling and sieving. The obtained powders were calcined at 1200 °C for 6 h. The XRD diffraction of the SrTi<sub>1-x</sub>Fe<sub>x</sub>O<sub>3-δ</sub> powders correspond to cubic SrTiO<sub>3</sub>, card no. 35-0734, with no indication of impurities or second phases (Fig. 1A). Grain size of the obtained powder as seen in HR-SEM was approximately 1 μm (Fig. 10A). The presence and quantity of iron in SrTiO<sub>3</sub> was verified by calculating the band-gap energy from UV-vis reflection (Fig. 1B) and by EDS for selected powders. For specimen preparation, 4 wt% of polyvinyl alcohol (PVA) in water was added to the STO/STFO powders. Rectangular compact powder was uniaxial pressed in stainless steel die at 6.9 MPa followed by a cold isostatic press of 193 MPa. The PVA binder was burnt out at 500 °C for 10 min. The green body specimen dimensions were 10 mm by 3 mm by 3 mm with density of ~60% of the theoretical density.

### 2.2. Methods

#### 2.2.1. Heat balance model- solution method

The sample temperature is assumed uniform in space (lumped system) and it is governed by heat generation, radiation, convection and conduction. The heat balance and the control volume description are given in Eq. (4) and Fig. 2 respectively:

$$\frac{d}{dt} (mC_p T_s) = q_{gen} - q_{loss} \quad (4)$$

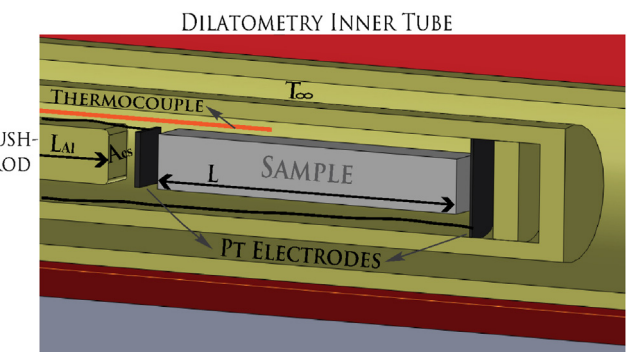


**Fig. 2.** Illustration of the control volume and the assembly of the experimental system that was modeled here. The sample is a  $10 \times 3 \times 3$  mm<sup>3</sup> rectangular compact powder. On both edges, electrodes of 400 nm Pt are sputtered. The sample is held between Pt foils: a static one from the right and connected to the dilatometer push-rod from the left. These electrodes enable both to measure the sample impedance and to apply an electric field. In practice, sample temperature is measured by the thermocouple located 1 mm above the center of the sample. This is referred to as sample thermocouple temperature,  $\tilde{T}_s$ , in the experimental part, as opposed to  $T_s$  which is the average temperature used in the heat balance model.

where: t, m, C<sub>p</sub>, T<sub>S</sub>, q<sub>gen</sub> and q<sub>loss</sub> are the time, sample mass, heat capacity, sample temperature, generated heat and heat losses respectively.

The heat generation in the system is caused by the electrical current (Joule heating) and is given by:

$$q_{gen} = IV = \frac{V^2}{R(T_s)} = I^2 R(T_s) \quad (5)$$

where: I, V and R(T<sub>s</sub>) are the electrical current, potential difference and the temperature dependent sample resistance respectively. The heat losses in the system are influenced by radiation, convection and conduction through the dilatometer push-rod (Fig. 2). These terms are given by:

$$q_{loss} = \underbrace{\varepsilon \sigma A (T_s^4 - T_\infty^4)}_{\text{radiation}} + \underbrace{h A (T_s - T_\infty)}_{\text{convection}} + \underbrace{q_{cond}}_{\text{conduction}} \quad (6)$$

**Table 1**

Values of the different parameters set for the calculation of the conduction term.

Parameter	Units	Value	
m	gr	0.2	Measured
C <sub>p</sub>	J/kgK	500	Measured (see 2.2.3)
ε	–	0.9	reference <sup>6</sup>
σ	W/m <sup>2</sup> K <sup>4</sup>	5.67·10 <sup>8</sup>	Stefan-Boltzmann constant
A	mm <sup>2</sup>	120	area exposed to convection and radiation
h	W/m <sup>2</sup> K	20	Calculation were based on natural convection correlation

where:  $\epsilon$ ,  $\sigma$ ,  $h$ ,  $A$ ,  $T_\infty$  are emissivity factor, Stephan-Boltzmann constant, convection coefficient, surface area that is exposed to convection and radiation and furnace temperature. The conduction term was calculated at two different methods in stages I and III. The values for the different parameters are shown in Table 1. At stage I, the conduction term is time dependent and calculated according to semi-infinite body model (Eq. (7.1)). At stage III, a steady state stage, the conduction term is time independent and calculated according to infinite fin model (Eq. (7.2)) [26].

$$q_{cond}(t) = (T_s - T_\infty) A_{cs} \sqrt{\frac{k\rho C_p}{\pi t}} \quad (7.1)$$

$$q_{cond} = (T_s - T_\infty) \sqrt{khpA_{cs}} \quad (7.2)$$

where  $k$ ,  $\rho$  and  $C_p$ ,  $A_{cs}$  and  $p$  are the conduction coefficient, density, heat capacity, and push-rod cross-section area and perimeter of the alumina push-rod respectively.

As opposed to convection and radiation, the calculation of the conduction term varies between the different stages. At all stages, part of the heat transferred from the sample to the dilatometer push-rod is released from it to the furnace through convection and radiation mechanisms. However, during the first and second transient stages, part of that energy accumulates in the push-rod, elevating its temperature. In order to calculate accurately these contributions, one has to simulate the dilatometer push-rod using a spatial, time dependent model. Since the purpose here is to construct an accurate yet simple as possible model for calculating the onset temperature, the following technique was used. In the first stage, the conduction term was calculated according to semi-infinite body model, whereas at the steady state stage (stage III) an infinite-fin model was used. However, calculation based on this procedure while assuming perfect contact between the sample and the alumina push-rod, would result in over-estimation of the heat transfer through conduction. Hence, a correction due to imperfect contact should be estimated for the term of heat loss by conduction. Optimizing different experimental data with the simulations suggest that roughly 40% of the total conduction term should be used. This value of 40% is an adjustable parameter that was set after several iterations of model and experimental data. It is only suitable to this specific system and should be modified when another system is used. The contribution of conduction via the two Pt electrodes was found negligible in comparison to the total conduction, thus it was not included in the calculations.

In order to solve the heat balance in stage I, the following finite differences approximation was used for the time derivative:

$$\frac{d}{dt} (mC_p T_s) = mC_p \frac{dT_s}{dt} \cong mC_p \frac{T_{s,i+1} - T_{s,i}}{\Delta t} \quad (8)$$

Using Eq. (8) in the heat balance (Eq. (4)) yields:

$$mC_p \frac{T_{s,i+1} - T_{s,i}}{\Delta T} = \frac{V^2}{R(T_{s,i})} - \epsilon\sigma A(T_{s,i}^4 - T_\infty^4) - hA(T_{s,i} - T_\infty) - q_{cond}(t) \quad (9)$$

$$\text{Or : } T_{s,i+1} = T_{s,i} + \frac{\Delta T}{mC_p} \left[ \frac{V^2}{R(T_{s,i})} - \epsilon\sigma A(T_{s,i}^4 - T_\infty^4) - hA(T_{s,i} - T_\infty) - q_{cond}(t) \right] \quad (9)$$

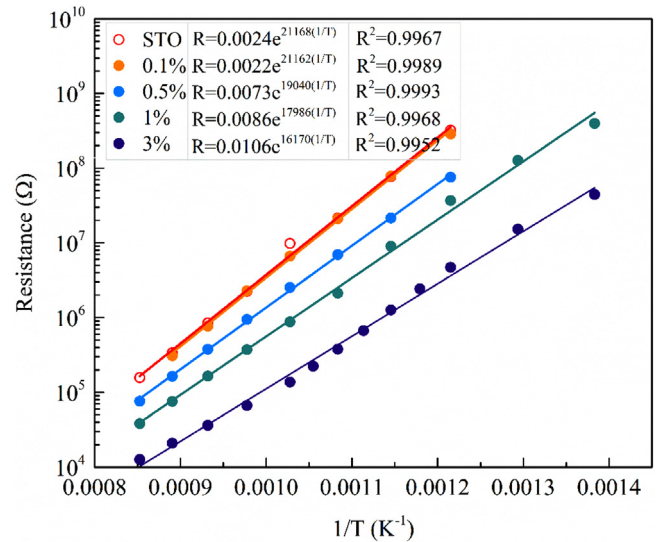


Fig. 3. Arrhenius plots for five different green compact samples of STFO. The undoped STO and 0.1% iron doped plots are almost identical.

For each sample of STFO, resistance as a function of temperature was measured separately. The corresponding Arrhenius approximation (Fig. 3) was used for the calculation. The activation energies decrease with doping, in accordance with the band gap decrease observed in Fig. 1B. At the first step ( $t=0$ ), the sample temperature is equal to the furnace temperature ( $T_s = T_\infty$ ), and the sample resistance, the heat generation and current were calculated according to the applied voltage (V). At the i-th step, the sample temperature is used to find the resistance, and the new sample temperature  $T_{s,i+1}$  is calculated using Eq. (8). The flash sintering onset condition is defined by the current compliance of the experimental system. In our system, this value was 100 mA (current density of ~11 mA/mm<sup>2</sup>).

The third stage of flash sintering can be treated as time independent where all the parameters in Eq. (4) (heat generation and losses) are constant.

## 2.2.2. Electrical measurements

Impedance spectroscopy measurements were carried out using BioLogic SP-200 potentiostat with frequency range of 0.1 Hz–1 MHz, 10 points per decade. The stimulus voltage amplitude was 1 V. The total resistance was evaluated from the constant value at the lower frequencies.

## 2.2.3. Specific heat

The specific heat values of the sample,  $C_p(T)$ , were calculated from thermal conductivity measurements of STFO porous samples in a Netzsch LFA-457, laser flash analyzer (LFA). Heat capacity is derived from a model using comparison with an alumina standard. Since the values for different STFO samples varied in the range of 450–540 J/kg · K, and changed the obtained onset temperatures

by 1–5 °C only, an average value of 500 J/kg·K was used in the simulation.

#### 2.2.4. HR-SEM

High resolution scanning electron microscopy, HR-SEM, imaging was performed using a Zeiss Ultra Plus high resolution scanning electron microscope, equipped with a Schottky field-emission electron gun and a Gemini electron-beam column. Energy dispersive X-ray spectrometer (Oxford Instruments EDX detector with resolution of 127 eV, operated at acceleration voltages of 10–20 keV) was used for phase verification and chemical compositional analysis.

#### 2.2.5. UV-vis

Optical band gap was established by diffuse reflectance measurements using the Cary 5000 UV-vis-NIR spectrophotometer (Agilent Technologies) with a DRA-2500 integrating sphere attachment. Optical reflection was obtained over a range of 250–1000 nm.

#### 2.2.6. XRD

Rigaku miniflex diffractometer with CuK $\alpha$  beam was used for XRD measurements. Operating conditions were 30 kV and 15 mA and the scanning range was 20–80° using scan rate of 2°/min. The step size was 0.01° per step ( $2\theta$ ).

#### 2.2.7. Atmosphere control

The oxygen partial pressure was adjusted by mixing pure Ar with a mixture of 50% Ar-50% O<sub>2</sub> at specific molar ratios. All gases had certificates for 99.995% purity from their manufacturer. The gas mixture enters the sealed dilatometer at a constant total flow rate.

#### 2.2.8. Dilatometry

Dilatometry measurements preformed in a differential horizontal furnace configuration dilatometer (TA DIL-802) with maximal temperature of 1700 °C.

#### 2.2.9. Flash sintering measurements

The flash sintering setup is assembled in a modified horizontal furnace configuration dilatometer (TA DIL-801) with maximal temperature of 1500 °C, taking advantage of its ability to measure shrinkage in-situ (details are described elsewhere [1]). DC Electrical field is applied to the electrodes via three Keithley 2400 source meters connected in series to achieve maximum voltage of 600 V with limiting current of 100 mA.

Both dilatometers (TA DIL-801 and DIL-802) have two thermocouples, one located at the center of the furnace, referred to as furnace temperature; the second is located 1 mm above the center of sample and referred to as sample thermocouple temperature  $\tilde{T}_s$ ; note it is not the same as the sample average temperature. This distinction between the sample average temperature and  $\tilde{T}_s$  becomes prominent under applied field during flash sintering experiments, not only because it is measured at a small distance from the sample, but more importantly due to the temperature distribution within the sample. However, in the absence of electric field these two temperatures are considered the same.

### 3. Results

#### 3.1. Predicting the onset temperature by an energy balance model for the in-situ dilatometry system

Heat generation and losses components during incubation are shown in Fig. 4 for the undoped STO case. The main contributions are the heat generation and heat losses by radiation, while conduction (under the assumption of non-ideal contact mentioned in the experimental section) and convection losses are two orders of magnitude lower. The incubation stage terminates at the maximal

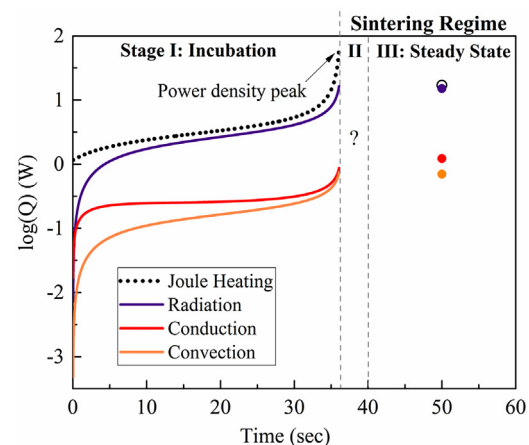


**Fig. 4.** The change of energy balance components (logarithmic scale) in time for undoped STO. The three distinguished area of flash sintering are marked with dashed lines.

power density peak; afterwards the sintering regime begins. The sintering regime is composed of the transient stage, namely the switching from voltage to current control that lasts less than a second, and a steady state regime. Raj [6] showed that sintering regime initiate at the transient (switching) and include a sample temperature increase and changes in the power density. Afterwards the system reaches a quasi-steady state in which the sample temperature remains higher than in incubation, the power density stabilizes and the sample shrinkage is very moderate. In the experimental work (Fig. 9 Section 3.2.2),  $\tilde{T}_s$ , the powder density behavior and the linear shrinkage enable the separation of stage 2 and 3, as shown in Raj work. After the transition, stage 2, the power density is unstable and  $\tilde{T}_s$  keeps increasing. Only when these two parameters become constant, accompanied with a moderate linear shrinkage (constant slope) the system reaches a quasi-steady state. Since stage 2 is characterized by a large dynamic change in the sample dimensions and in the sample resistance, this regime could not be simulated here. It is marked in a question mark in Fig. 4. It should be mentioned that during incubation, thermal expansion of the sample is well observed by the dilatometer (Fig. 8 Section 3.2.2). Unlike the significant change in length at flash sintering (ranging between 6 and 18% linear shrinkage), changes due to thermal expansion are smaller (approximately 0.5%) and negligible in this simulation. In the third (steady state) regime, the values of all contributing parameters are constant and shown as dots in Fig. 4.

Since our experimental instruments are limited to a maximal voltage of 600 V/cm (maximal power of 60 W), we used this model to predict the onset temperatures at different applied fields for all STFO samples (Fig. 5). The correlation of the electric field with the onset temperature behave as a power law. This behavior was shown before for YSZ [14,27] and BaTiO<sub>3</sub> [11,28], obeying a similar power law. YSZ and STO differ in their electrical conductivity mechanism. The fact that in both cases similar power law behavior is observed can imply that the onset temperatures of flash are determined mainly by the resistance-temperature dependency of the sample. This is further supported by the fact that enhancing iron doping levels in the STFO enhance the conductivity as well as the oxygen vacancy concentrations and reduce the onset temperature, but does not change the general power-law behavior.

Comparison between the simulation and experimental results of onset temperatures (Fig. 6), show a similar trend in which the onset temperature decreases with increasing iron doping in STO. This result is further elaborated in the experimental part 3.2, where the contribution of oxygen vacancy and electronic charge carrier concentrations are discussed. The simulation results are higher by

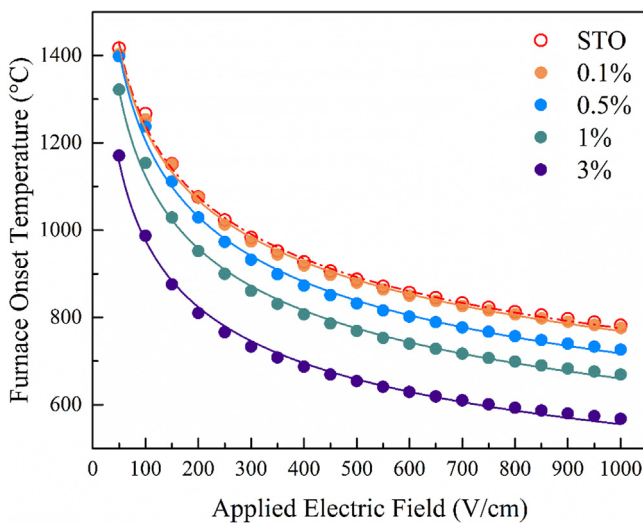


**Fig. 5.** Furnace onset temperature as a function of applied electric field calculated from the model for all STFO samples.

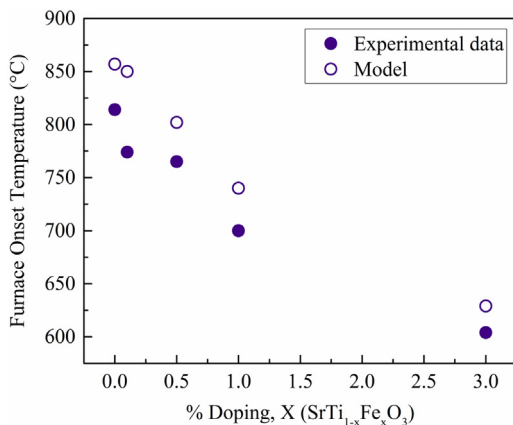


**Fig. 6.** Furnace onset temperatures, simulation results and experimental data at applied field of 600 V/cm.

25–50 °C as compared to the experimental results. That can be explained by the model approximation in which the sample temperature is considered without internal gradients. It was shown that the conductivity inside the sample during flash is highly significant and generates large temperature variance. This cause the sample core to reach very high temperatures, while the edges are significantly colder than the average temperature. Since in this model the sample temperature is assumed as constant, the envelope temperature is higher in the model than in reality, the heat losses (mainly by radiation, but also by convection and conduction) are higher and result in higher onset temperatures. Practically, the model deviation is consistent, and one can relate it to assess the furnace onset temperature merely by measuring the compact green body ceramic resistance.

### 3.2. The role of point defects on the onset conditions of flash sintering—experimental part

#### 3.2.1. The influence of oxygen vacancies on the initial stage of conventional sintering

The influence of oxygen vacancies on the first stage of sintering is demonstrated by shrinkage behavior of different STFO samples during temperature rise (Fig. 7). When increasing iron doping, the ionic compensation by oxygen vacancies is dominant (see Eq. (3)) and

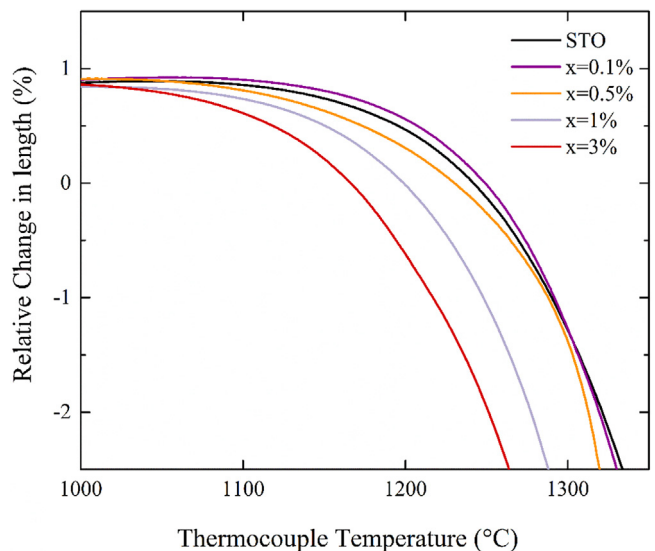


**Fig. 7.** Dilatometry measurement of the shrinkage behavior of STFO samples during temperature increase. The plot is a zoom-in of the area at which early stage of sintering is observed. No shrinkage was observed below 1000 °C.

their concentration increases, resulting in sintering commences at significantly lower temperatures. The fact that the oxygen activity, rather than the acceptor itself, is the important factor in such systems has been established previously [17]. While SrTi<sub>1-x</sub>Fe<sub>x</sub>O<sub>3-δ</sub> forms a continuous solid solution between SrTiO<sub>3</sub> and SrFeO<sub>3</sub>, in this work SrTi<sub>0.97</sub>Fe<sub>0.03</sub>O<sub>2.985</sub> was chosen as the highest amount of iron doping. At samples with iron content x < 3%, the samples can be treated as 'dilute solution', having no interaction between point defects. Early stage sintering of the highly doped sample, SrTi<sub>0.97</sub>Fe<sub>0.03</sub>O<sub>2.985</sub>, is evident at 1000 °C, a significantly lower temperature than for the undoped sample. It should be noted that when performing flash sintering experiments at high temperatures (>1100 °C), the sample is already in the early-stage sintering regime and the green body microstructure is deformed. This complicates the analysis of FAST sintering (type A), which is done with lower field and at higher temperatures as compared to flash [29]. This change could also be a result of changes in the microstructure of the different STFO specimens. However, since no substantial changes were observed in grain size or shape we postulate that the increase in the oxygen vacancies concentration results in the temperature reduction of the early stage sintering.

#### 3.2.2. The behavior of STFO below and above the onset conditions in isothermal experiments

In the isothermal experiment, the furnace temperature was raised in steps of 50 °C, while at each step the applied field was increased by steps of 100 V/cm, ranging from 100 to 600 V/cm (Fig. 8). Three different responses are evident (marked as cases 1–3). At low fields (usually lower than 200 V/cm), the linear shrinkage and  $\tilde{t}_s$  are constant and no response is monitored in neither (case 1). In that case the current is very low, at the order of the open circuit value. Nevertheless, at elevated temperatures such fields should cause a minor Joule heating effect that would result in FAST sintering behavior, as observed previously [28,29]. In case 2 we do see response in all measured parameters. The sample expands and its temperature rises; the current moderately increases, but remains far below the instrument compliance (in this case 100 mA or 11 mA/mm<sup>2</sup>). The electric field was held until the current reaches a steady value. Removal of the field results in sample shrinkage back to the original size, indicating that the expansion is due to the heating induced by the current. Only above a threshold field (case 3), the

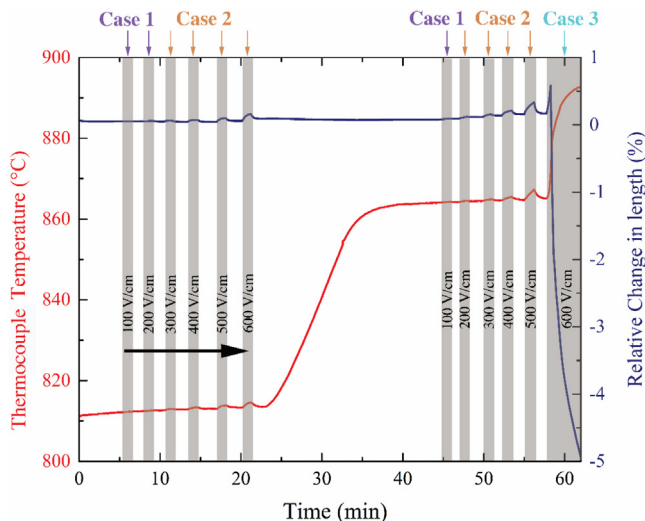


**Fig. 8.**  $\tilde{T}_s$  and relative change in length in time domain. Every grey vertical stripe represents an electric field pulse in the range of 100–600 V/cm. The response in terms of sample length and temperature (as measured 1 mm above the sample center) are shown. Three main responses are observed. Case 1- no visible response; Case 2- thermal expansion and an increase of temperature are observed but the flash sintering does not occur; Case 3- flash sintering: higher thermal expansion and temperature increase, results in switching of the system and sample shrinkage.

sample expansion is enhanced (between 0.5–0.8% relative change in length), the current reaches the source compliance and the system alters from voltage control to current control following with an abrupt linear shrinkage. Case 3 describes the phenomenon of flash sintering (type B), were the sintering regime begins with the system switching. Fig. 9 shows an example of STO flash sintering

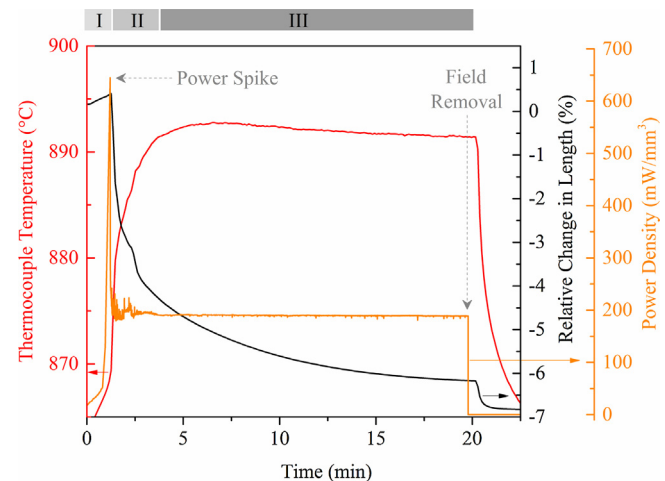


**Fig. 9.** Flash sintering experiment at furnace temperature of 850 °C and 600 V/cm. The linear shrinkage,  $\tilde{T}_s$  and power density show a typical behavior of flash sintering divided into three distinguished areas. The first is the incubation stage (I) accompanied with a nonlinear increase in the sample conductivity. When the sample conductivity reaches the instrument compliance, it alters from voltage to current control; this stage is called the transient stage (II). Lastly, under current control, a steady-state regime is characterized with a constant power density and sample length. After the removal of the field, the temperature decreases and another sharp shrinkage is observed due to the sample thermal shock.

at 850 °C and 600 V/cm. The shrinkage behavior and  $\tilde{T}_s$  are plotted together with the power density during the electric field pulse. The known three regimes of incubation, transition and steady-state are shown in this flash fingerprint plot. The separation between stage 2 and 3 is discussed in Section 3.1.

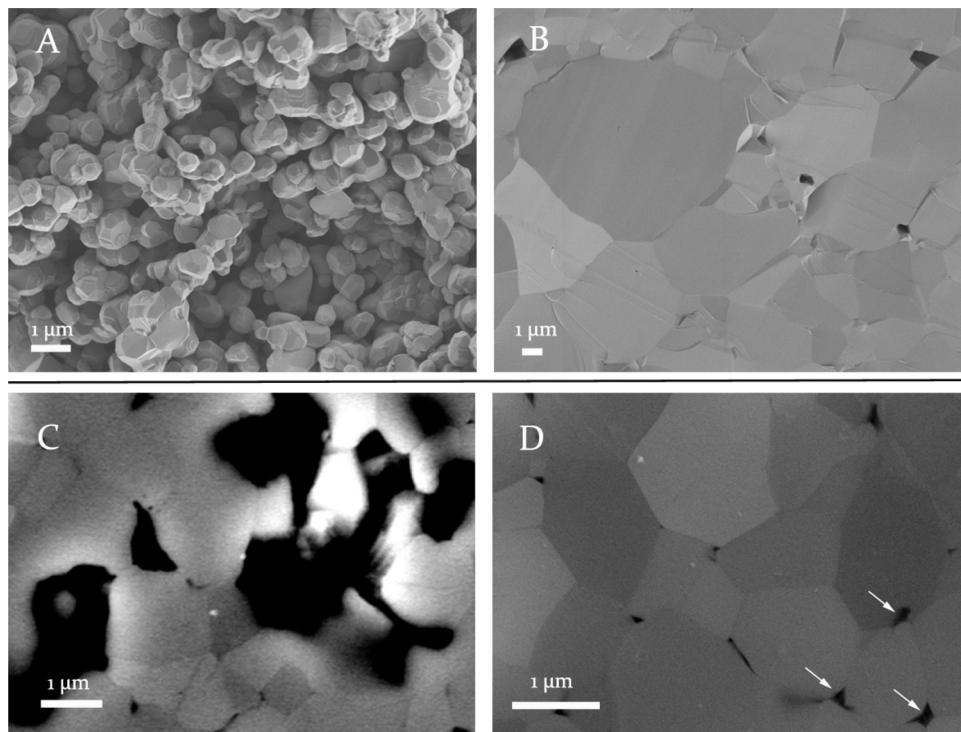


**Fig. 10.** HR-SEM images (A) STO powder with average grain size of 1  $\mu\text{m}$ ; (B) cross-section image of STO after conventional sintering at 1450 °C for 8 h. Significant grain growth is observed as grain size range between 4 and 9  $\mu\text{m}$ . (C) and (D) are cross-section images of STO after flash sintering at the onset temperature (the experimental data shown in Fig. 5). (C) A highly porous area located close the electrode edge, and (D) The internal area of the sample. The image was taken from the center of the specimen, and represents very well the dense sample after polishing the porous envelop of the sample. This area contains closed pores (see arrows). No significant grain growth is evident after flash sintering.

The STO sample obtained from flash sintering at the onset condition was sintered in its major internal part. The homogeneity of a sintered ceramic is an important parameter which influences the material properties. In the geometry used here, a rectangular sample, the obtained sample is distorted and is characterized by a non-dense envelope and a dense ‘core’ (Supplementary materials, SM, Fig. S1.1). A dense sample is obtained after polishing all six facets and removing the non-dense envelope. The final density, after polishing is higher than 90% of the theoretical density. The average grain size of the initial powder is 1 μm (HR-SEM Fig. 10A). A significant grain growth is evident after conventional sintering at 1450 °C for 8 h (HR-SEM Fig. 10B). The HR-SEM images after flash sintering at the onset condition demonstrate that the area located close the Pt electrode is highly porous (Fig. 10C), while a homogeneous dense material with some distributed small and closed pores is seen in the rest of the sample (Fig. 10D). The grain size after flash sintering in both porous and dense areas is similar to that of the initial powder (average grain size of 1 μm) with no significant grain growth.

It should be mentioned here that while in conventional sintering, the linear shrinkage of STO is approximately 15% and the shrinkage is uniform in all directions (see dilatometry measurement in SM Fig. S2.1), in the flash sintering experiments the linear shrinkage at the onset temperature is around 5%. The reason is the inhomogeneity of the sample as explained above. In the isothermal experiments, the sample resistance is measured before and after applying the electric field. There was a decrease in the sample resistance by an order of magnitude after the removal of the field at the end of the flash process. This change is an additional evidence of sample densification.

### 3.2.3. Finding the onset temperature of STFO in non-isothermal conditions at constant field

In non-isothermal experiments, Fig. 11, the furnace temperature was moderately increased by 2°/min while applying a constant electric field of 600 V/cm. This was set according to the onset electric field found in the isothermal experiments described in the previous section. The spike in thermal expansion and the sudden rise of the sample temperature are both synchronized with a spike of power, as shown in Fig. 9 (in this experiment it was not recorded due to technical limitations). The current in the spike reaches its compliance of 100 mA. At that point the furnace onset temperature and  $\tilde{T}_s$  can be identified.

The furnace and sample onset temperatures reduce with increasing iron doping (Fig. 12). The behavior of the furnace onset temperature as a function of iron content has been predicted by the heat balance model (Fig. 6, Section 3.1). The decrease in onset temperature with elevating iron doping can be explained solely via the decrease in green body resistance. This decrease in green body resistance is due to increasing oxygen vacancy concentration. Consequently, the contribution of point defects to the assumed enhanced mass transport should be evaluated while the oxygen vacancy concentration is constant, and the resistance changes result from changes of the concentration of holes.

To achieve conditions where the oxygen vacancy concentration is constant while the resistance is significantly changed, the following STFO property is utilized. In highly doped STFO, the Brouwer approximation to the neutrality equation reads:

$$[V_O^{\cdot\cdot}] \cong \frac{1}{2} [Fe'_n] \quad (10)$$

Thus, the oxygen vacancy concentration is pinned over a large range of pO<sub>2</sub> as well as at all relevant temperatures. From the redox reaction and its corresponding mass action relation:

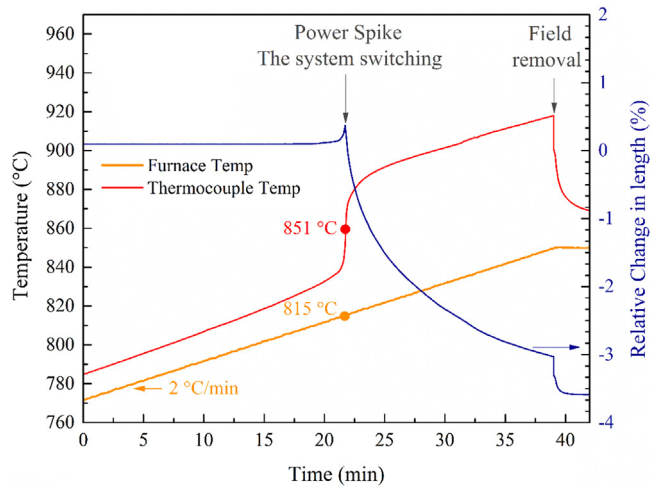
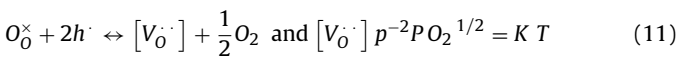


**Fig. 11.** A voltage of 600 V is applied to the sample while increasing the furnace temperature in a rate of 2 °C/min. In that way, the furnace onset temperature can be found accurately, while  $\tilde{T}_s$  is measured in situ during the three stages of flash.  $\tilde{T}_s$  marked by a dot is the value measured at the system switching. The thermal response appeared in Fig. 5 after removing the electric field is seen here as well.

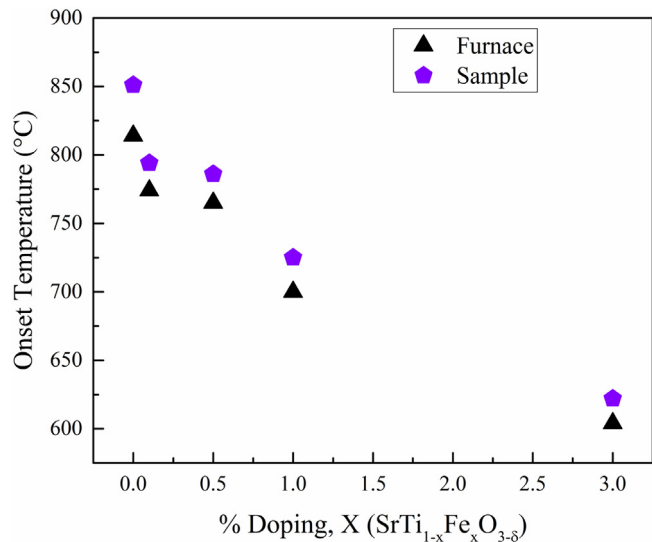


**Fig. 12.**  $\tilde{T}_s$  and furnace onset temperature as a function of increasing iron doping at applied field of 600 V/cm.

as long as the oxygen vacancy concentration is pinned by the dopants, the following relations hold:

$$\frac{p}{n} \propto P(O_2)^{\pm 1/4} \quad (12)$$

The hole concentration is the important one at the higher oxygen partial pressure regime [21,30,31].

The highly doped sample used in this study was SrTi<sub>0.97</sub>Fe<sub>0.03</sub>O<sub>2.985</sub>. In this experimental work, both the resistance and the onset temperature were found at different pO<sub>2</sub>. Fig. 13 shows that increasing the green body conductance by enhancing pO<sub>2</sub>, the furnace onset temperature (at constant field of 600 V/cm) is decreased. Since the oxygen vacancy concentration is fixed by Eq. (10), at both relevant pO<sub>2</sub> and temperature ranges, the mass transfer has a constant contribution here, even when induced by the field. Therefore, the result shown in Fig. 13 suggests that the major parameter influencing the onset temperature is the sample resistance.

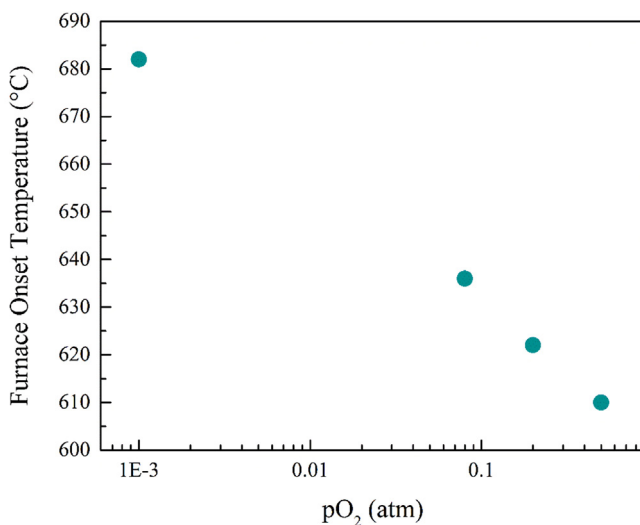


**Fig. 13.** Furnace onset temperature as a function of oxygen partial pressure. When increasing the  $pO_2$ , the sample resistance decreases solely by the increase of hole concentration, while the oxygen vacancy concentration remains constant.

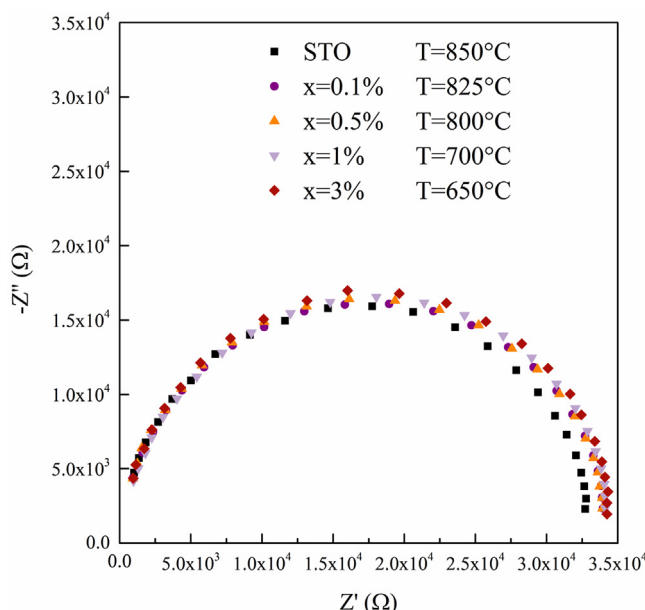


**Fig. 14.** Nyquist plot of STFO green samples at temperatures close to  $\tilde{T}_s$  that was found in the non-isothermal experiment (Fig. 12). At these temperatures, the resistance of all samples is equal and the impedance plots exhibit a single overlapping semicircle.

### 3.2.4. Ex-situ impedance spectroscopy measurements of green samples close to the onset temperatures

In the previous section it was shown that the onset temperature is influenced by the sample resistance even when the ionic defect concentrations are kept constant. Next, we examine the electrical properties of different samples without field, at temperatures that are in the vicinity of the threshold. This is done by a two-point impedance spectroscopy measurement on samples at steady state, (Fig. 14). It is evident that the sample resistances are almost identical. Moreover, the Cole–Cole (Nyquist) plots contain one overlapping semicircle for all of the samples. Although in-situ and ex-situ measurements of the resistance at  $\tilde{T}_s$  are significantly different, the overlapping data indicate that there is a threshold resistance of the green body below which flash can occur. This threshold resistance is achieved at lower temperatures as doping

increases. The appearance of only one semicircle at these temperatures indicate one process in the material within the bandwidth that contribute to the total impedance. In all those samples, the in situ resistance at the power spike is  $6\text{ k}\Omega$ , while the ex situ value is  $\sim 35\text{ k}\Omega$ . This discrepancy is expected at least since at the spike the sample temperature is non uniform and certainly much higher locally than the average. Other differences may also contribute.

## 4. Conclusions

- (1) The simulation presented here, can predict the furnace onset temperature at different applied voltages, simply by using the green sample resistance as a function of temperature. The simulation predictions are slightly higher than the experimental obtained data, mainly because the sample temperature is assumed uniform. This assumption magnifies the heat losses and consequently results in higher onset temperatures. The deviation between the model and the data is constant, and enables one to evaluate the real furnace onset temperature. The onset temperature – applied field relations obey a power law as was shown before by other models and experimental results for oxide ceramics. The fact that a similar power law was found for YSZ, a material with different conduction mechanism, reinforce the fact that the onset temperature is determined by the sample resistance.
- (2) It is known that the oxygen activity influences the sintering commence in oxide perovskites. This behavior was examined and reinforced here for STFO. However, the influence of ionic defects on the onset temperature and the initiation of flash was under debate. In STFO, the point defect concentrations can be pinned and the resistance is influenced by the oxygen partial pressure through electronic carriers. The furnace onset temperatures of 3% iron doped STFO at different  $pO_2$  were examined at several high oxygen pressures, where the sample is a p-type semiconductor. The onset temperatures were found from non-isothermal experiments. Additionally, the different responses of the sample at lower temperatures and fields were examined in isothermal experiments. The onset temperature decreases with increasing  $pO_2$  and the resulting conductivity.
- (3) Ex-situ impedance measurements of different green bodies having various doping levels overlap close to the sample onset temperature. It can be concluded that the transition between the incubation and transient stages is determined by the green body resistance regardless how it has been achieved. It is expected, however, that at the transient stage the ionic defects have a direct impact on the flash process.

## Acknowledgments

Support from the Nancy and Stephen Grand Technion Energy Program (GTEP), the ISF INREP center and grant no. 938/15 and the BSF are gratefully acknowledged. S.B. wishes to thank the Center for Absorption in Science and the Ministry of Immigrant Absorption for their support.

## Appendix A. Supplementary data

Supplementary data associated with this article can be found, in the online version, at <http://dx.doi.org/10.1016/j.jeurceramsoc.2016.07.037>.

## References

- [1] N. Shomrat, S. Baltianski, C.A. Randall, Y. Tsur, Flash sintering of potassium-niobate, *J. Eur. Ceram. Soc.* 35 (2015) 2209–2213.

- [2] R. Muccillo, E.N.S. Muccillo, An experimental setup for shrinkage evaluation during electric field-assisted flash sintering: application to yttria-stabilized zirconia, *J. Eur. Ceram. Soc.* 33 (2013) 515–520.
- [3] M.C. Steil, D. Marinha, Y. Aman, J.R.C. Gomes, M. Kleitz, From conventional ac flash-sintering of YSZ to hyper-flash and double flash, *J. Eur. Ceram. Soc.* 33 (2013) 2093–2101.
- [4] J.S.C. Francis, M. Cologna, R. Raj, Particle size effects in flash sintering, *J. Eur. Ceram. Soc.* 32 (2012) 3129–3136.
- [5] A. Karakuscu, et al., Defect structure of flash-sintered strontium titanate, *J. Am. Ceram. Soc.* 95 (2012) 2531–2536.
- [6] R. Raj, Joule heating during flash-sintering, *J. Eur. Ceram. Soc.* 32 (2012) 2293–2301.
- [7] M. Cologna, B. Rashkova, R. Raj, Flash sintering of Nanograin Zirconia in <5 s at 850 °C, *J. Am. Ceram. Soc.* 93 (2010) 3556–3559.
- [8] Y. Dong, I. Chen, Onset criterion for flash sintering, *J. Am. Ceram. Soc.* 3627 (2015) 3624–3627.
- [9] Y. Dong, I. Chen, Predicting the onset of flash sintering, *J. Am. Ceram. Soc.* 98 (2015) 2333–2335.
- [10] S. Grasso, et al., Modeling of the temperature distribution of flash sintered zirconia, *J. Ceram. Soc. Jpn.* 119 (2011) 144–146.
- [11] J. Gustavo, H.A. Al-qureshi, F. Keil, R.A. Janssen, dynamic bifurcation criterion for thermal runaway during the flash sintering of ceramics, *J. Eur. Ceram. Soc.* 36 (2016) 1261–1267.
- [12] T.B. Holland, U. Anselmi-tamburini, D.V. Quach, T.B. Tran, A.K. Mukherjee, Effects of local Joule heating during the field assisted sintering of ionic ceramics, *J. Eur. Ceram. Soc.* 32 (2012) 3667–3674.
- [13] I.J. Hewitt, A.A. Lacey, R.I. Todd, A mathematical model for flash sintering, *Math. Model. Nat. Phenom.* 10 (2015) 77–89.
- [14] R.I. Todd, R.S. Bonilla, T. Sneddon, P.R. Wilshaw, Electrical characteristics of flash sintering: thermal runaway of Joule heating, *J. Eur. Ceram. Soc.* 35 (2015) 1865–1877.
- [15] Y. Zhang, J. Jung, J. Luo, Thermal runaway, flash sintering and asymmetrical microstructural development of ZnO and ZnO–Bi2O3 under direct currents, *Acta Mater.* 98 (2015) 87–100.
- [16] J. Narayan, A new mechanism for field-assisted processing and flash sintering of materials, *Scr. Mater.* 10 (2013) 107–111.
- [17] R.D. Levi, Y. Tsur, The effect of oxygen vacancies in the early stages of BaTiO<sub>3</sub> nanopowder sintering, *Adv. Mater.* 17 (2005) 1606–1608.
- [18] S. Steinsvik, R. Bugge, J.O.N. Gjonnes, J. Tafto, T. Norby, The defect structure of SrTi<sub>1-x</sub>Fe<sub>x</sub>O<sub>3-y</sub> (x=0–0.8) investigated by electrical conductivity measurements and electron energy loss spectroscopy (EELS), *J. Phys. Chem. Solids* 58 (1997) 969–976.
- [19] N.H. Perry, J.J. Kim, S.R. Bishop, H.L. Tuller, Strongly coupled thermal and chemical expansion in the perovskite oxide system Sr(Ti,Fe)O<sub>3- $\alpha$</sub> , *J. Mater. Chem. A Mater. Energy Sustain.* 3 (2015) 3602–3611.
- [20] A. Rothschild, W. Meneskou, H.L. Tuller, E. Ivers-tiffé, Electronic structure, defect chemistry, and transport properties of SrTi<sub>1-x</sub>Fe<sub>x</sub>O<sub>3-y</sub> solid solutions, *Chem. Mater.* 18 (2006) 3651–3659.
- [21] R. Moos, K.H. Hardtl, Defect chemistry of donor-doped and undoped strontium titanate ceramics between 1000 °C and 1400 °C, *J. Am. Ceram. Soc.* 80 (1997) 2549–2562.
- [22] A. Karakuscu, et al., Defect structure of flash-sintered strontium titanate, *J. Am. Ceram. Soc.* 2536 (2012) 2531–2536.
- [23] N. Shomrat, D. Haviv, Y. Tsur, The correlation between non-stoichiometry and charge compensation in perovskites, *J. Electroceram.* 33 (2014) 135–141.
- [24] Y. Tsur, I. Riess, Self-compensation in semiconductors, *Phys. Rev. B* 860 (1999) 8138–8146.
- [25] M. Hammer, M. Hoffmann, Sintering model for mixed-oxide-derived lead zirconate titanate ceramics, *J. Am. Ceram. Soc.* 81 (1998) 3277–3284.
- [26] F.P. Incropera, D.P. Dewitt, *Fundamentals of Heat and Mass Transfer*, NY Wiley, Hoboken, 2011.
- [27] J.A. Downs, V.M. Sgavio, I. Industriale, Electric field assisted sintering of cubic zirconia at 390 °C, *J. Am. Ceram. Soc.* 96 (2013) 1342–1344.
- [28] J.M. Peko, J.S.C. Francis, R. Raj, Field-assisted sintering of undoped BaTiO<sub>3</sub>: microstructure evolution and dielectric permittivity, *J. Eur. Ceram. Soc.* 34 (2014) 3655–3660.
- [29] S.K. Jha, R. Raj, The effect of electric field on sintering and electrical conductivity of titania, *J. Am. Ceram. Soc.* 97 (2013) 527–534.
- [30] Y. Tsur, C.A. Randall, Charge-Compensation in BaTiO<sub>3</sub>, Proc. 12th IEEE Int. Symp. Appl. Ferroelectr. Eds., S.K. Streiffer, B.J. Gibbons T. Tsurumi, IEEE 1, 151–154 (2001).
- [31] Y. Tsur, C.A. Randall, Point defect concentrations in barium titanate revisited, *J. Am. Ceram. Soc.* 49 (2001) 2147–2149.